

Article

Magnetic Field-Induced Resistivity Upturn and Non-Topological Origin in the Quasi-One-Dimensional Semimetals

Yalei Huang , Rongli Ye, Weihao Shen, Xinyu Yao  and Guixin Cao * 

Materials Genome Institute, Shanghai University, Shanghai 200444, China

* Correspondence: guixincao@shu.edu.cn

Abstract: As a layered topological nodal line semimetals hosting a quasi-one-dimensional (quasi-1D) crystalline structure, TaNiTe₅ has attracted intensive attention. In this research, we analyze the low temperature (low-*T*) transport properties in single crystals of TaNiTe₅. The high anisotropic transport behaviors confirm the anisotropic electronic structure in quasi-1D TaNiTe₅. The resistivity shows a magnetic field-induced resistivity upturn followed by a plateau at low temperatures when current is parallel to the *c* axis and magnetic field is parallel to the *b* axis. An extremely large magnetoresistance of 1000% has been observed at 2 K and 13 T. Such a magnetic field-induced phenomenon can be generally explained using the topological theory, but we find that the behaviors are well accounted with the classical Kohler's rule. The analysis of the Hall resistivity points to carrier compensation in TaNiTe₅, fully justifying Kohler's rule. Our findings imply that analogous magnetic field-induced low-*T* properties in nodal line semimetals TaNiTe₅ can be understood in the framework of classical magnetoresistance theories that do not require to invoke the topological surface states.

Keywords: topological semimetals; resistivity plateau; extremely large magnetoresistance; Kohler's rule



check for updates

Citation: Huang, Y.; Ye, R.; Shen, W.; Yao, X.; Cao, G. Magnetic Field-Induced Resistivity Upturn and Non-Topological Origin in the Quasi-One-Dimensional Semimetals. *Symmetry* **2023**, *15*, 1882. <https://doi.org/10.3390/sym15101882>

Academic Editors: Alexey V. Lukoyanov and Jim Freericks

Received: 18 August 2023
Revised: 23 September 2023
Accepted: 2 October 2023
Published: 7 October 2023



Copyright: © 2023 by the authors. Licensee MDPI, Basel, Switzerland. This article is an open access article distributed under the terms and conditions of the Creative Commons Attribution (CC BY) license (<https://creativecommons.org/licenses/by/4.0/>).

1. Introduction

Topological semimetals (TSMs) with nontrivial band structures have been one of the spotlights in condensed matter physics owing to their novel topological responses [1–4]. Compared with high-dimensional materials, low-dimensional materials, especially one-dimensional materials, exhibit unique characteristics due to the quantum confinement effect [5–7]. For instance, when electrons are spatially confined to a quasi-1D bismuthine edge, the system is in the Tomonaga–Luttinger liquid regime, with the characteristic feature of the separation of charge and spin [8]. Due to the anisotropic one-dimensional conductive channels, backscattering is strictly prohibited in quasi-1D materials, which favors the generation of highly directional spin currents and contributes to the development of spintronics devices with low energy consumption [9]. Therefore, the TSM with low-dimensional structures provided an excellent platform to explore and engineer topological properties due to the reduced dimensionality. Nevertheless, a vast majority of TSMs identified to date are two-dimensional or three-dimensional, whereas one-dimensional TSMs have rarely been identified.

As topological material candidates with quasi-1D structural characteristics, ternary transition-metal telluride has attracted intensive attention [9–15]. For example, the ABTe₄ (A = Nb, Ta; B = Ir, Rh) family has been predicted to be a new series of type-II Weyl semimetals [12,16]. Experimentally, the Shubnikov-de Haas oscillations have been observed as in TaIrTe₄ [11] and NbIrTe₄ [17], which indicate the light effective masses of charge carriers and the nontrivial Berry phase associated with Weyl fermions. In addition, the Fermi arcs as well as Weyl nodes in the bulk of TaIrTe₄ have been identified directly via angle-resolved photoemission spectroscopy (ARPES) [18,19]. Interestingly, on the TaIrTe₄ surface, quasi-1D superconductivity has been observed [19], illustrating the strong correlation between complex quantum phenomena and quasi-1D structure. From a crystal structure viewpoint,

both NbIrTe₄ and TaIrTe₄ have a layered non-centrosymmetric orthorhombic structure with alternating quasi-1D IrTe₂ and NbTe₂/TaTe₂ chains along *a* axis [20,21]. It is worth noting that this structural feature is very common in ternary transition-metal telluride [13]. Therefore, the structural similarities and complicated topological properties in ternary transition metal tellurides have prompted further exploration of novel topological materials in these low-dimensional compounds.

Another new family in ternary transition metal tellurides, Ta-based TaXTe₅ (X = Ni, Pd, Pt) has been recently proposed as candidates for quasi-1D topological materials that possess stable chemical properties [15,22,23]. Among them, TaNiTe₅ has the similar layered orthorhombic structure [24,25]. Its eclipsed stacking of the atomic layer is along the *b* axis through van der Waals interactions, and the alternating one-dimensional TaTe₃ and NiTe₂ chains are parallel to *a* axis in the layered slab. The quasi-1D properties and topological electronic structures of TaNiTe₅ have been well investigated. The quasi-1D atomic nature of the surface and the electronic structures in TaNiTe₅ have been characterized using scanning tunneling microscopy/spectroscopy. The cryogenically cleaved TaNiTe₅ is terminated with quasi-1D stripes along the crystallographic *a* axis, and the spatial distribution of local density of states exhibits apparent anisotropy [26]. Moreover, the quasi-one-dimensionality of TaNiTe₅ has also been demonstrated because of its large anisotropy in the resistivity [27]. The excellent quasi-1D electronic properties of TaNiTe₅ would inspire low-dissipation devices and applications. In our previous study, we have found a pronounced de Haas–van Alphen oscillations and revealed three major oscillation frequencies, $F_1 = 56$ T, $F_2 = 162$ T, and $F_3 = 232$ T, under $\mu_0 H // b$, and two major oscillation frequencies, $F_4 = 64$ T, and $F_5 = 252$ T, under $\mu_0 H // a$, respectively [27]. The corresponding light effective masses and the nontrivial Berry phases suggest the nontrivial band topology in TaNiTe₅. The ARPES and density functional theory (DFT) calculations revealed multiple Dirac-type nodal lines with fourfold degeneracy in TaNiTe₅, which results from the interplay between non-symmorphic symmetry and structural anisotropy [28]. Further, ARPES and spin-resolved ARPES combined with DFT calculations revealed the coexistence of the strong and weak topological phases in TaNiTe₅ [9], where the surface states protected by weak topological order forms Dirac-node arcs in the vicinity of the Fermi energy, which are responsible for the strong anisotropy in the transport measurements [9]. Furthermore, on the surface of TaNiTe₅, the ferroelectric-like polarization and novel surface states have been obtained via ARPES, scanning tunneling microscopy and piezo response force microscopy measurements [29]. The interesting combination of ferroelectric-like polarization and novel surface states has intriguing potential for future applications. These studies demonstrate that the TaXTe₅ (X = Ni, Pd, Pt) family is a promising platform to investigate low-dimensional quantum phenomena and further facilitates the development of spintronics.

A recent study showed magnetic field-induced resistivity upturn and plateau in TaNiTe₅ [23], which shows that its origin from a field-induced metal-to-insulator-like transition. Similar resistivity upturn and plateau in topological insulator materials under zero magnetic field have been widely investigated, like Bi₂Te₂Se [30] and SmB₆ [31]. In the topological insulators, the surface that is in contact with air is metallic, whereas the bulk states are completely gapped out near the Fermi level [32,33]. The metallic surface states are protected by time reversal symmetry (TRS), and thus are robust to disorders. The hallmark of transport signature of surface states in the topological insulators displays a typical resistivity plateau [30,31,34], which arrests the exponential divergence of the insulating bulk with decreasing temperature. On the other hand, similar resistivity upturn and plateau have been investigated in topological semimetals under magnetic field [32,35–40]. Several mechanisms have been proposed to explain these features [32,35–37,40–42]. Tafti et al. observed resistivity upturn followed by a plateau at low temperatures when $\mu_0 H \geq 0.5$ T in LaSb [32], which is related to the breaking of TRS in topological semimetals; that is, the magnetic field-induced resistivity upturn is generally considered indicative of a metal–insulator transition resulting from the gap opening at the band-touching points, and the resistivity plateau is consid-

ered as a transport signature for topological surface states [32,35,41,43]. However, in the case of Weyl semimetals WTe_2 , whose low- T upturn excludes the possible existence of a metal–insulator transition or a contribution of electronic structure change [40], indicative of the classical magnetoresistance (MR) origin. As a matter of fact, the sample which follows Kohler’s rule generally has residual resistivity, high mobilities, and large residual resistance ratio (RRR). The Kohler’s rule compliance indicates that the scattering mechanism remains the same throughout the related temperature and field ranges, which rules out the mechanism of a metal-to-insulator transition. A similar phenomenon in other topological semimetals have been explained with this mechanism, like YSb [37], TaSe₃ [36], and TaSb₂ [44]. Therefore, the magnetic field-induced metal–insulator transition is not the only mechanism to understand low- T resistivity upturn and plateau in topological semimetals. In this case, it is critical to explore the origin of the low- T magnetic field-induced behaviors in TaNiTe₅.

In this research, high-quality TaNiTe₅ single crystals were grown to study the transport properties. The transport behavior for TaNiTe₅ is highly anisotropic, which reflects its anisotropic electronic properties of quasi-1D structure. When $I//c$ and $\mu_0 H//b$, magnetic field-induced resistivity upturn and plateau are observed, and an extremely large magnetoresistance (XMR) is observed. The magnetic field-induced behaviors can be accounted with the classical magnetoresistance theory, i.e., Kohler’s rule. The analysis of magnetic field dependence of Hall resistivity shows electron–hole compensation in TaNiTe₅. The relatively low carrier concentrations and high mobility characteristic are consistent with the nature of topological semimetal for TaNiTe₅. Our result provides strong support for the magnetic field-induced properties in TaNiTe₅ without the necessity of invoking topologically nontrivial states.

2. Experimental and Methods

As we know, high-quality single crystals serve as the premise and foundation for investigating novel physical properties, and the crystal quality significantly affects the transport properties [32]. This effect is even more obvious in the topological materials because the quantum phenomenon is sensitive to crystal quality [32,45]. In order to observe the intrinsic transport properties of the topological material, it is essential to prepare high-quality single-crystal samples. Compared to the chemical vapor transport method, single crystals grown using the self-flux method generally display fewer defects and impurities. On the other hand, the high RRR value is a good indicator of excellent crystal quality. For example, the RRR of self-flux-grown WTe_2 crystals reaches a value of 1256, which is much higher than the values of 184–370 of the sample grown using the chemical vapor transport method [45–47]. In addition, the cooling rate has a great influence on the crystal quality in the self-flux method. A slow cooling rate is advantageous for obtaining high-quality single crystals. Thus, high-quality TaNiTe₅ single crystals were grown using the self-flux method. The powder of Ta (99.99%), Ni (99.99%), and Te (99.99%) were mixed with the molar ratio 1:1:10 and placed in an alumina crucible. The crucible was sealed in a silica tube under vacuum. The quartz tube was heated in a furnace at 1000 °C for 32 h, and then cooled to 500 °C with 1 K/h cooling rate. At 500 °C, the silica tube was centrifuged to separate the crystals from the flux. TaNiTe₅ single crystals with metallic luster were finally obtained. The inset of Figure 1b shows the typical size of the samples. The single crystals were examined using a x-ray diffractometer (XRD, Bruker, D2, Germany). The chemical compositions were characterized via energy-dispersive x-ray spectroscopy (EDX, FlexSEM-1000, Hitachi, Japan). The chemical composition of the crystals utilized was determined to be TaNi_{1.1}Te_{5.5}, which is very close to the ideal chemical composition. Henceforth, we refer to the obtained samples as TaNiTe₅. All samples were removed from the remaining flux on the surface, and fashioned into bar-shaped samples. The electrical transport properties were carried out in a commercial physical property measurement system (PPMS, Quantum Design). The standard four-probe method was employed for the electrical measurements. The Hall resistivity was obtained by subtracting the longitudinal resistivity component.

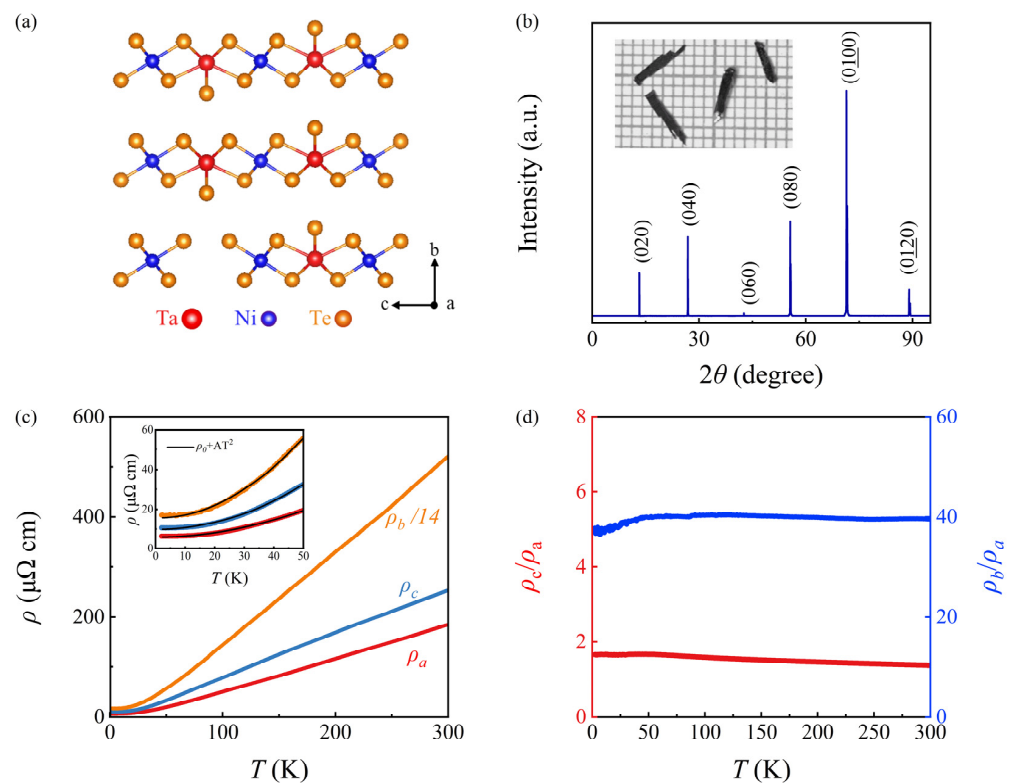


Figure 1. (a) Crystal structure of TaNiTe₅ viewed along the *a* axis. (b) XRD pattern of single crystal. Inset: Typical optical image of TaNiTe₅ single crystals. (c) Temperature dependence of the electronic resistivity ρ_a , ρ_b , and ρ_c , with current applied along *a* axis, *b* axis, and *c* axis, respectively, for TaNiTe₅. The inset shows the enlarged view of ρ_a , ρ_b , and ρ_c in the low-*T* regime and the fit to the Fermi liquid paradigm. (d) Temperature dependence of the resistivity anisotropy for ρ_c/ρ_a and ρ_b/ρ_a , respectively.

3. Results and Discussion

TaNiTe₅ crystallizes in the orthorhombic space group (*Cmcm*, No.63) with the refined lattice parameter $a = 3.659 \text{ \AA}$, $b = 13.122 \text{ \AA}$, $c = 15.111 \text{ \AA}$, and $\alpha = \beta = \gamma = 90^\circ$ [24]. As depicted in Figure 1a, triangle NiTe₂ chains are formed along *a* axis, making the compound structurally one-dimensional and exhibit highly anisotropic behaviors. Figure 1b shows the XRD patterns collected from an as-grown facet of TaNiTe₅ single crystals. It can be seen that only the (0*l*0) Bragg peaks are observed, demonstrating that the exposed surface is *ac* plane. Figure 1c displays the temperature (*T*) dependence of resistivity measured at zero field with current along three crystallographic axes, i.e., $\rho_a(T)$, $\rho_b(T)$, and $\rho_c(T)$, respectively. The residual resistivity ratio $\text{RRR} = \rho(300 \text{ K})/\rho(2 \text{ K})$ are $\text{RRR}_a = 30$, $\text{RRR}_b = 24$, $\text{RRR}_c = 31$, respectively. These values are much bigger than the value reported so far [23,25]. $\rho_a(T)$, $\rho_b(T)$, and $\rho_c(T)$ all show an approximate linear temperature dependence between 300 and 50 K. Upon further cooling, all of them gradually deviate from linear dependence, and cross over to a quadratic temperature dependence at low-temperature region, as demonstrated in the inset of Figure 1c; that is, the data of three directions can be described with the Fermi liquid, suggesting that electron–electron scattering mechanism dominates in the low-*T* region. Figure 1d shows that the temperature dependence of resistivity anisotropy of TaNiTe₅. The small value of $\rho_c/\rho_a \sim 1.4\text{--}1.7$ during the whole temperature range of 2–300 K suggests a weak anisotropy in the layered slab. By contrast, the value of $\rho_b/\rho_a \sim 37\text{--}39$ is much bigger than that of $\rho_c/\rho_a \sim 1.4\text{--}1.7$, which demonstrates the strong anisotropy between in-plane and out-of-plane. Evidently, the quasi-1D transport behaviors in TaNiTe₅ are clearly manifested by $\rho_a:\rho_b:\rho_c = 1:28:1.4$ at 300 K and $1:27:1.7$ at 2 K, respectively. A similar anisotropic behavior also appears in the sister compounds TaPdTe₅ [13], and TaPtTe₅ [22]. The anisotropic transports signify the large anisotropic Fermi surfaces and the associated electron lifetime, reflecting its quasi-1D electronic structure. Notably, the anisotropy value

of our sample is the highest compared to the previous report [23]. Both the RRR value and highest anisotropy assure the high quality of our single crystals.

Based on our high-quality single crystals of TaNiTe₅, we further measured the temperature-dependent resistivity along each direction of the crystallographic axis under various magnetic fields. As shown in Figure 2a–c, $\rho_a(T)$, $\rho_b(T)$, and $\rho_c(T)$ display interesting anisotropy behavior. Both $\rho_a(T)$ and $\rho_b(T)$ show typical metallic behavior with negligible MR until applied field of 13 T. By contrast, $\rho_c(T)$ shows metallic behavior at high temperatures, while the resistivity reached a minimum at T_m once $\mu_0 H \geq 6$ T. Remarkably, below T_m , the resistivity keeps increasing until a resistivity plateau is reached at T_i . A similar anisotropic behavior has been observed in its sister compound TaPdTe₅ [22] and NbNiTe₅ [15], which reflects the anisotropic electronic properties in this quasi-1D material. To obtain the values of T_m and T_i , we plotted the temperature dependence of the derivative $d\rho_c/dT$ under various magnetic fields, as shown in the inset of Figure 2c. T_m is defined by the point where $d\rho_c/dT = 0$, and T_i is the point where $d\rho_c/dT = 0$ is minimum. Figure 2d shows the magnetic field dependence of T_m and T_i . T_m and T_i both increase monotonically with increasing magnetic field, while the increase in T_m is more drastic than that of T_i . And T_m is well fitted using the equation $T_m \propto (\mu_0 H - \mu_0 H_0)^{1/\nu}$, with fitting parameters $\nu = 1.73$. The value is close to those observed $\nu = 2$ in compensated semimetals WTe₂ [40], graphite [48], and bismuth [48]. It was predicted that at $T \leq T_m$ an excitonic gap can be induced by a magnetic field with $T_m \propto (\mu_0 H - \mu_0 H_0)^{1/2}$ [49], which was earlier used as an evidence of a metal–insulator transition. However, as shown in the inset of Figure 3, the MR curves decreases monotonically with increasing temperature without any gap-opening-induced features, such as steps at T_m . Furthermore, as shown in Figure 3, when MR curves at different magnetic fields are normalized with values at 2 K, all curves overlap each other. This is inconsistent with the case of a magnetic field-induced gap, where a steeper slope in MR curves would appear under a higher magnetic field [40,50]; that is, a metal–insulator transition is probably not the origin of the low- T resistivity upturn in our TaNiTe₅ crystals.

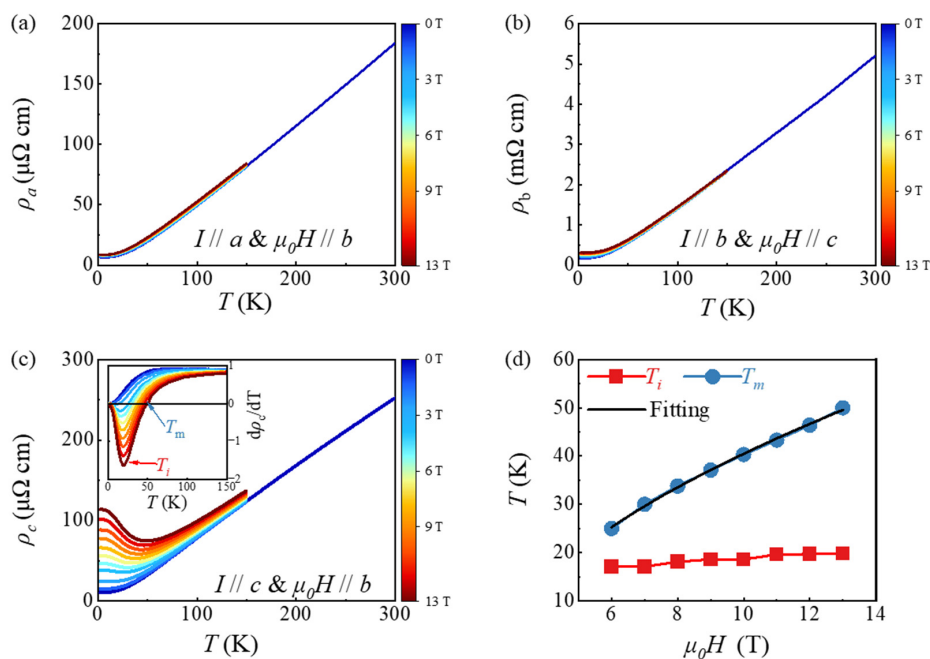


Figure 2. (a) Temperature dependence of electronic resistivity ρ_a with the magnetic field parallel to the b axis up to 13 T for TaNiTe₅. (b) Temperature dependence of electronic resistivity ρ_b with the magnetic field parallel to the c axis up to 13 T for TaNiTe₅. (c) Temperature dependence of electronic resistivity ρ_c with the magnetic field parallel to the b axis up to 13 T for TaNiTe₅. The inset shows the T_m and T_i values obtained from the differential curves under various fields. (d) T_m and T_i as a function of magnetic field. The black line is the fit to $T_m \propto (\mu_0 H - \mu_0 H_0)^{1/\nu}$.

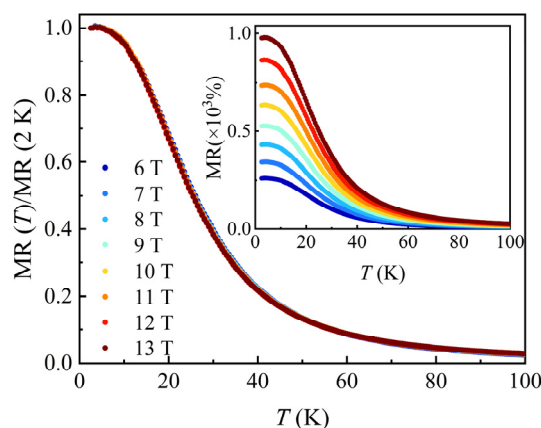


Figure 3. Temperature dependence of the normalized magnetoresistances obtained at various fixed magnetic fields with current parallel to the *c* axis and magnetic fields parallel to the *b* axis. Inset shows temperature dependence of the original magnetoresistances obtained at various magnetic fields with current parallel to the *c* axis and magnetic fields parallel to the *b* axis.

To further analyze the mechanism for the magnetic field-induced phenomenon in TaNiTe₅, we measured the magnetic field-dependent magnetoresistance at fixed temperatures with current parallel to the *c* axis and magnetic fields parallel to the *b* axis. MR is defined as $[\rho(\mu_0 H) - \rho(0 T)] / \rho(0 T)$, where $\rho(\mu_0 H)$ is the longitudinal resistivity under magnetic field, and $\rho(0 T)$ is the longitudinal resistivity at zero magnetic field. As shown in Figure 4a, we observe the XMR in TaNiTe₅, where MR reaches about 1000% at $T = 2$ K and $\mu_0 H = 13$ T without any sign of saturation. This is comparable to other XMR materials [36,42,51]. As we know, Kohler’s rule can describe the motion of electrons in a single band or multiple bands under magnetic field [40,52]. In previous studies on topological semimetal [36,40,44], the magnetic field-induced phenomenon could be explained within the framework of Kohler’s rule. Here, we use Kohler’s rule to analyze the MR curves. In Kohler’s rule,

$$MR = \alpha [\mu_0 H / \rho(0 T)]^m$$

where α and m are constants. When $m = 2$, the above-mentioned Kohler’s rule equation can be derived from the two-band model of electrical resistivity. The derived process is given below. The complex resistivity in the two-band model is expressed as [47,53]

$$\hat{\rho} = \frac{1 + \mu_e \mu_h \mu_0 H^2 + i(\mu_h - \mu_e) \mu_0 H^2}{e[n_e \mu_e + n_h \mu_h + i(n_e - n_h) \mu_e \mu_h \mu_0 H]}$$

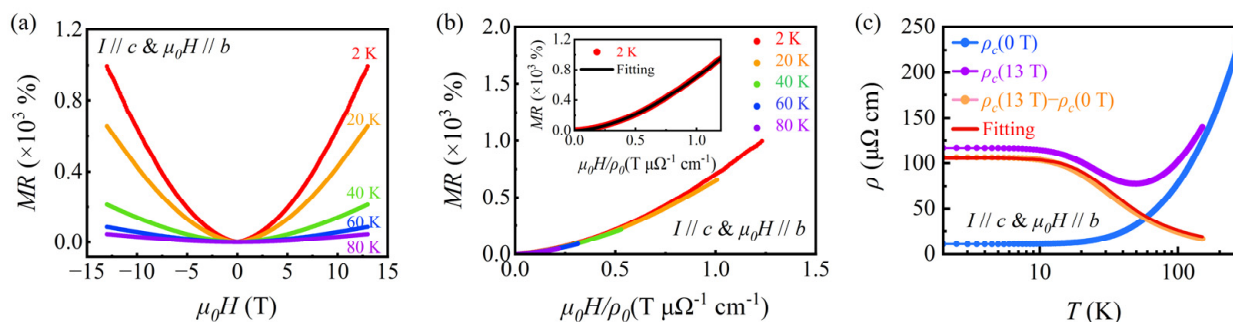


Figure 4. (a) The MR for ρ_c with the magnetic fields parallel to the *b* axis at selected temperatures for TaNiTe₅. (b) Kohler’s scaling for ρ_c at selected temperatures for TaNiTe₅. Inset: MR vs. $\mu_0 H / \rho_0$ at $T = 2$ K. The solid black line represents a fit to $MR = \alpha [\mu_0 H / \rho(0 T)]^m$. (c) Temperature dependence of resistivity ρ_c with the magnetic fields parallel to the *b* axis at 0 T and 13 T and their differences for TaNiTe₅. The solid red line represents fit to Kohler’s rule.

The experimentally observed resistivity equals to $Re\hat{\rho}$. When the system is in perfect electron–hole compensation, $n_e = n_h = n$, we can obtain

$$\rho(0 T) = [en(\mu_e + \mu_h)]^{-1}$$

and

$$\text{MR} = [\rho(\mu_0 H) - \rho(0 T)] / \rho(0 T) = \mu_h / \mu_e [ne(1 + \mu_h / \mu_e)]^{-2} (\mu_0 H / \rho(0 T))^2.$$

We define $\alpha = \mu_h / \mu_e [ne(1 + \mu_h / \mu_e)]^2$; thus, we obtain

$$\text{MR} = \alpha [\mu_0 H / \rho(0 T)]^2.$$

For the system with an imperfect compensated ($m \neq 2$), Kohler's rule can be still obeyed when the first two terms in the denominator in $\hat{\rho}$ dominates [40]. We note that in this case, $\alpha = \mu_h / \mu_e [e(n_e + \mu_h / \mu_e n_h)]^{-2}$, which is temperature-independent. In the case of temperature-dependent α , Kohler's rule would be violated [40]. As presented in Figure 4b, the MR curves from $T = 2$ –80 K can basically be scaled into a single curve when plotted as MR vs. $\mu_0 H / \rho(0 T)$; that is, the temperature dependence of the MR under $I // c$ and $\mu_0 H // b$ in TaNiTe₅ follows Kohler's rule, indicating that the scattering mechanism keeps same over the measured temperature and magnet field ranges. Thus, the possibility of an intrinsic field-induced metal–insulator transition can further be ruled out [40,54]. Inset of Figure 4b shows MR as a function of $\mu_0 H / \rho(0 T)$ at 2 K from which α and m were determined, $\alpha = 380 \left(\mu\Omega \text{ cm T}^{-1} \right)^m$ and $m = 1.7$. Kohler's rule can be rearranged and written as

$$\text{MR} = [\rho(\mu_0 H) - \rho(0 T)] / \rho(0 T) = \alpha [\mu_0 H / \rho(\mu_0 H = 0)]^m$$

i.e.,

$$\rho(\mu_0 H) = \rho(0 T) + \alpha \frac{\mu_0 H^m}{\rho(0 T)^{m-1}}$$

As seen, the resistivity under magnetic field consists of two terms, one is temperature dependence of the resistivity at zero field, i.e., $\rho(0 T)$, the other one is magnetic field-induced resistivity, i.e., $\alpha \frac{\mu_0 H^m}{\rho(0 T)^{m-1}}$. Evidently, the two terms have opposite dependence on temperature, so the competition between them lead to a minimum in resistivity under magnetic field [40,55,56]. Figure 4c shows the temperature dependence of resistivity ρ_c with $\mu_0 H // b$ at 0 T [$\rho(0 T)$] and 13 T [$\rho(13 T)$] and their differences [$\rho(13 T) - \rho(0 T)$], respectively. As seen, the differences $\rho(13 T) - \rho(0 T)$ is fitted with the second term, i.e., $\alpha \frac{\mu_0 H^m}{\rho(0 T)^{m-1}}$ with $\alpha = 380 \left(\mu\Omega \text{ cm T}^{-1} \right)^m$ and $m = 1.7$, as represented by the red solid line. The fitting further suggests that Kohler's rule is obeyed in TaNiTe₅. This indicates that the temperature dependence of the resistivity in a fixed magnetic field is solely determined by $\rho(0 T)$, because both α and m are temperature-independent. Furthermore, at low temperatures, $\rho(0 T)$ becomes low and almost independent of temperature variation. This implies $\rho(\mu_0 H) \sim \alpha \frac{\mu_0 H^m}{\rho(0 T)^{m-1}}$ at low temperatures, which is almost constant, giving rise to a resistivity plateau. Thus, the magnetic field-induced resistivity upturn and plateau in TaNiTe₅ can be explained with the help of the classical magnetoresistance theory; that is, while TaNiTe₅ is nodal-line semimetals, it is not necessary to invoke topological theories to explain the magnetic field-induced phenomenon. This case is similar to WTe₂ [40] and TaSe₃ [42].

To confirm the carrier type, concentration, and mobility in TaNiTe₅, the Hall effect was investigated. Figure 5a shows the results of Hall resistivity (ρ_H) at various temperatures. It can be seen that magnetic field-dependent Hall resistivity $\rho_H(\mu_0 H)$ deviates from a perfect linear behavior. This suggests that both electron and hole are responsible for the Hall effect, reflecting the multi-band characteristic in TaNiTe₅. For a system with multi-band,

$\rho_H(\mu_0 H)$ curves are fitted with the two-band model including both electron- and hole-type carriers [52]. In the two-band model, the experimentally observed Hall resistivity equals to $\text{Im}\hat{\rho}$ [47,52]:

$$\rho_H = \text{Im}\hat{\rho} = \frac{\mu_0 H}{e} \frac{(\mu_h^2 n_h - \mu_e^2 n_e) + (\mu_h \mu_e)^2 (\mu_0 H)^2 (n_h - n_e)}{(\mu_h n_h + \mu_e n_e)^2 + (\mu_h \mu_e)^2 (\mu_0 H)^2 (n_h - n_e)^2}$$

where $n_h(n_e)$ and $\mu_h(\mu_e)$ are density and mobility of holes (electrons), respectively. We fit our measured Hall resistivity ρ_H vs. $\mu_0 H$ as shown in Figure 5a. It can be seen that the fits are well performed with the nonlinear data below 100 K. The obtained values of n_h , n_e , μ_h , and μ_e are shown in Figure 5b. The result shows that n_h and n_e do not significantly change with temperature. At $T = 2$ K, n_h and n_e are evaluated to be $\sim 1.01 \times 10^{21} \text{ cm}^{-3}$ and $\sim 0.98 \times 10^{21} \text{ cm}^{-3}$, respectively. Simultaneously, the obtained μ_h and μ_e are $1.23 \times 10^4 \text{ cm}^2 \text{ V}^{-1} \text{ S}^{-1}$ and $7.70 \times 10^3 \text{ cm}^2 \text{ V}^{-1} \text{ S}^{-1}$ at $T = 2$ K, respectively. The relatively low carrier concentrations and high mobility characteristic are consistent with the nature of topological semimetal for TaNiTe₅. The ratio $n_h/n_e \sim 1.02$ – 1.05 , depending on the temperature, points towards a carrier compensation, which fully justifies Kohler's rule [40,42]. In addition, the results suggest that electron–hole resonance plays the dominant role for XMR in TaNiTe₅ when the magnetic field is applied. The case is similar to that in Weyl semimetal WTe₂ [40], in which Kohler's scaling takes into account magnetoresistance of normal metals that do not require topological surface states. Therefore, while the topological surface state is present in single crystals of TaNiTe₅, one does not need to invoke this to explain magnetic field-induced resistivity upturn and plateau at low temperatures.

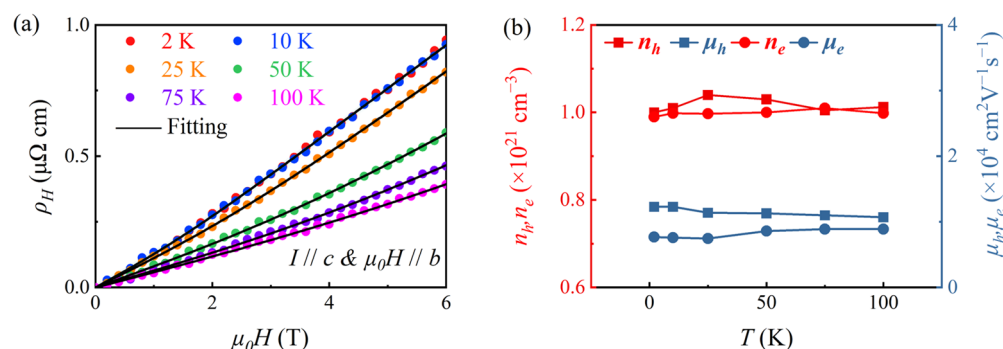


Figure 5. (a) The magnetic field dependence of Hall resistivity at various temperatures with current parallel to c axis and the magnetic field parallel to the b axis for TaNiTe₅. The black solid lines represent the two-band model fitting. (b) Temperature dependence of the carrier density and the mobility extracted from the above fits.

4. Conclusions

In summary, we present an experimental investigation of the transport magnetic properties of high-quality TaNiTe₅ single crystals, which show significant anisotropic behavior and have a quasi-1D structure. The resistivity $\rho_c(T)$ exhibits magnetic field-induced resistivity upturn and plateau at low- T regime when $\mu_0 H \geq 6$ T. XRM is observed, reaching 1000% at $T = 2$ K under $\mu_0 H = 13$ T. Through fitting, we found that the magnetic field-induced behaviors follow Kohler's rule. In addition, the analysis of the Hall effect points to electron–hole compensation in TaNiTe₅, making Kohler's rule fully justified. The results imply that classical magnetoresistance theories can be used to explain the magnetic field-induced properties in topological materials.

Author Contributions: Methodology, Y.H. and R.Y.; Investigation, W.S. and X.Y.; Writing—original draft preparation, Y.H.; Writing—review and editing, G.C.; Supervision, G.C.; Project administration, G.C. All authors have read and agreed to the published version of the manuscript.

Funding: This work was supported by Key Research Project of Zhejiang Lab (No. 2021PE0AC02) and Department of Science and Technology of Zhejiang Province (2023C01182). A portion of this work was performed at the Steady High Magnetic Field Facilities, High Magnetic Field Laboratory, CAS.

Data Availability Statement: Data available upon request from the authors.

Conflicts of Interest: The authors declare no conflict of interest.

References

1. Li, P.; Qiu, P.; Xu, Q.; Luo, J.; Xiong, Y.; Xiao, J.; Aryal, N.; Li, Q.; Chen, L.; Shi, X. Colossal Nernst power factor in topological semimetal NbSb₂. *Nat. Commun.* **2022**, *13*, 7612. [[CrossRef](#)]
2. Burkov, A.A. Topological semimetals. *Nat. Mater.* **2016**, *15*, 1145–1148. [[CrossRef](#)]
3. Bernevig, B.A.; Felser, C.; Beidenkopf, H. Progress and prospects in magnetic topological materials. *Nature* **2022**, *603*, 41–51. [[CrossRef](#)]
4. Chen, L.; Setty, C.; Hu, H.; Vergniory, M.G.; Grefe, S.E.; Fischer, L.; Yan, X.; Eguchi, G.; Prokofiev, A.; Paschen, S.; et al. Topological semimetal driven by strong correlations and crystalline symmetry. *Nat. Phys.* **2022**, *18*, 1341–1346. [[CrossRef](#)]
5. Noguchi, R.; Takahashi, T.; Kuroda, K.; Ochi, M.; Shirasawa, T.; Sakano, M.; Bareille, C.; Nakayama, M.; Watson, M.D.; Yaji, K.; et al. A weak topological insulator state in quasi-one-dimensional bismuth iodide. *Nature* **2019**, *566*, 518–522. [[CrossRef](#)]
6. Lin, C.; Ochi, M.; Noguchi, R.; Kuroda, K.; Sakoda, M.; Nomura, A.; Tsubota, M.; Zhang, P.; Bareille, C.; Kurokawa, K.; et al. Visualization of the strain-induced topological phase transition in a quasi-one-dimensional superconductor TaSe₃. *Nat. Mater.* **2021**, *20*, 1093–1099. [[CrossRef](#)]
7. Jiao, W.-H.; Xiao, S.; Zhang, S.-J.; Yang, W.-Z.; Xie, X.-M.; Liu, Y.; Liu, J.-Y.; Song, S.-J.; Liu, W.; Ren, Z.; et al. Structure and transport properties of the quasi-one-dimensional telluride Ta_{1.2}Os_{0.8}Te₄. *Phys. Rev. B* **2022**, *105*, 064201. [[CrossRef](#)]
8. Stühler, R.; Reis, F.; Müller, T.; Helbig, T.; Schwemmer, T.; Thomale, R.; Schäfer, J.; Claessen, R. Tomonaga–Luttinger liquid in the edge channels of a quantum spin Hall insulator. *Nat. Phys.* **2020**, *16*, 47–51. [[CrossRef](#)]
9. Wang, D.-Y.; Jiang, Q.; Kuroda, K.; Kawaguchi, K.; Harasawa, A.; Yaji, K.; Ernst, A.; Qian, H.-J.; Liu, W.-J.; Zha, H.-M.; et al. Coexistence of Strong and Weak Topological Orders in a Quasi-One-Dimensional Material. *Phys. Rev. Lett.* **2022**, *129*, 146401. [[CrossRef](#)]
10. Schönemann, R.; Chiu, Y.-C.; Zheng, W.; Quito, V.L.; Sur, S.; McCandless, G.T.; Chan, J.Y.; Balicas, L. Bulk Fermi surface of the Weyl type-II semimetallic candidate NbIrTe₄. *Phys. Rev. B* **2019**, *99*, 195128. [[CrossRef](#)]
11. Khim, S.; Koepernik, K.; Efremov, D.V.; Klotz, J.; Förster, T.; Wosnitza, J.; Sturza, M.I.; Wurmehl, S.; Hess, C.; van den Brink, J.; et al. Magnetotransport and de Haas–van Alphen measurements in the type-II Weyl semimetal TaIrTe₄. *Phys. Rev. B* **2016**, *94*, 165145. [[CrossRef](#)]
12. Liu, J.; Wang, H.; Fang, C.; Fu, L.; Qian, X. van der Waals Stacking-Induced Topological Phase Transition in Layered Ternary Transition Metal Chalcogenides. *Nano Lett.* **2017**, *17*, 467–475. [[CrossRef](#)]
13. Jiao, W.-H.; Xie, X.-M.; Liu, Y.; Xu, X.; Li, B.; Xu, C.-Q.; Liu, J.-Y.; Zhou, W.; Li, Y.-K.; Yang, H.-Y.; et al. Topological Dirac states in a layered telluride TaPdTe₅ with quasi-one-dimensional PdTe₂ chains. *Phys. Rev. B* **2020**, *102*, 075141. [[CrossRef](#)]
14. Xiao, S.; Jiao, W.-H.; Lin, Y.; Jiang, Q.; Yang, X.; He, Y.; Jiang, Z.; Yang, Y.; Liu, Z.; Ye, M.; et al. Dirac nodal lines in the quasi-one-dimensional ternary telluride TaPtTe₅. *Phys. Rev. B* **2022**, *105*, 195145. [[CrossRef](#)]
15. Jiao, W.-H.; Xiao, S.; Liu, W.; Liu, Y.; Qiu, H.-Q.; Xia, K.; He, S.; Li, Y.; Cao, G.-H.; Xu, X. Anisotropic transport and multiple topology in quasi-one-dimensional ternary telluride NbNiTe₅. *Phys. Rev. B* **2023**, *107*, 195124. [[CrossRef](#)]
16. Koepernik, K.; Kasinathan, D.; Efremov, D.V.; Khim, S.; Borisenko, S.; Büchner, B.; van den Brink, J. TaIrTe₄: A ternary type-II Weyl semimetal. *Phys. Rev. B* **2016**, *93*, 201101. [[CrossRef](#)]
17. Zhou, W.; Li, B.; Xu, C.Q.; van Delft, M.R.; Chen, Y.G.; Fan, X.C.; Qian, B.; Hussey, N.E.; Xu, X. Nonsaturating Magnetoresistance and Nontrivial Band Topology of Type-II Weyl Semimetal NbIrTe₄. *Adv. Electron. Mater.* **2019**, *5*, 1900250. [[CrossRef](#)]
18. Belopolski, I.; Yu, P.; Sanchez, D.S.; Ishida, Y.; Chang, T.-R.; Zhang, S.S.; Xu, S.-Y.; Zheng, H.; Chang, G.; Bian, G.; et al. Signatures of a time-reversal symmetric Weyl semimetal with only four Weyl points. *Nat. Commun.* **2017**, *8*, 942. [[CrossRef](#)]
19. Xing, Y.; Shao, Z.; Ge, J.; Luo, J.; Wang, J.; Zhu, Z.; Liu, J.; Wang, Y.; Zhao, Z.; Yan, J.; et al. Surface superconductivity in the type II Weyl semimetal TaIrTe₄. *Natl. Sci. Rev.* **2019**, *7*, 579–587. [[CrossRef](#)]
20. Mar, A.; Ibers, J.A. Synthesis and physical properties of the new layered ternary tellurides M₂IrTe₄ (M = Nb, Ta), and the structure of NbIrTe₄. *J. Solid State Chem.* **1992**, *97*, 366–376. [[CrossRef](#)]
21. Mar, A.; Jobic, S.; Ibers, J.A. Metal-metal vs tellurium-tellurium bonding in WTe₂ and its ternary variants TaIrTe₄ and NbIrTe₄. *J. Am. Chem. Soc.* **1992**, *114*, 8963–8971. [[CrossRef](#)]
22. Jiao, W.-H.; Xiao, S.; Li, B.; Xu, C.; Xie, X.-M.; Qiu, H.-Q.; Xu, X.; Liu, Y.; Song, S.-J.; Zhou, W.; et al. Anisotropic transport and de Haas–van Alphen oscillations in quasi-one-dimensional TaPtTe₅. *Phys. Rev. B* **2021**, *103*, 125150. [[CrossRef](#)]
23. Xu, C.; Liu, Y.; Cai, P.; Li, B.; Jiao, W.; Li, Y.; Zhang, J.; Zhou, W.; Qian, B.; Jiang, X.; et al. Anisotropic Transport and Quantum Oscillations in the Quasi-One-Dimensional TaNiTe₅: Evidence for the Nontrivial Band Topology. *J. Phys. Chem. Lett.* **2020**, *11*, 7782–7789. [[CrossRef](#)]
24. Liimatta, E.W.; Ibers, J.A. Synthesis, structures, and conductivities of the new layered compounds Ta₃Pd₃Te₁₄ and TaNiTe₅. *J. Solid State Chem.* **1989**, *78*, 7–16. [[CrossRef](#)]

25. Chen, Z.; Wu, M.; Zhang, Y.; Zhang, J.; Nie, Y.; Qin, Y.; Han, Y.; Xi, C.; Ma, S.; Kan, X.; et al. Three-dimensional topological semimetal phase in layered TaNiTe₅ probed by quantum oscillations. *Phys. Rev. B* **2021**, *103*, 035105. [[CrossRef](#)]
26. Ma, N.; Wang, D.-Y.; Huang, B.-R.; Li, K.-Y.; Song, J.-P.; Liu, J.-Z.; Mei, H.-P.; Ye, M.; Li, A. Quasi-one-dimensional characters in topological semimetal TaNiTe₅. *Chin. Phys. B* **2023**, *32*, 056801. [[CrossRef](#)]
27. Ye, R.; Gao, T.; Li, H.; Liang, X.; Cao, G. Anisotropic giant magnetoresistance and de Haas–van Alphen oscillations in layered topological semimetal crystals. *AIP Adv.* **2022**, *12*, 045104. [[CrossRef](#)]
28. Hao, Z.; Chen, W.; Wang, Y.; Li, J.; Ma, X.-M.; Hao, Y.-J.; Lu, R.; Shen, Z.; Jiang, Z.; Liu, W.; et al. Multiple Dirac nodal lines in an in-plane anisotropic semimetal TaNiTe₅. *Phys. Rev. B* **2021**, *104*, 115158. [[CrossRef](#)]
29. Li, Y.; Ran, Z.; Huang, C.; Wang, G.; Shen, P.; Huang, H.; Xu, C.; Liu, Y.; Jiao, W.; Jiang, W.; et al. Coexistence of Ferroelectric-like Polarization and Dirac-like Surface State in TaNiTe₅. *Phys. Rev. Lett.* **2022**, *128*, 106802. [[CrossRef](#)]
30. Ren, Z.; Taskin, A.A.; Sasaki, S.; Segawa, K.; Ando, Y. Large bulk resistivity and surface quantum oscillations in the topological insulator Bi₂Te₂Se. *Phys. Rev. B* **2010**, *82*, 241306. [[CrossRef](#)]
31. Kim, D.J.; Xia, J.; Fisk, Z. Topological surface state in the Kondo insulator samarium hexaboride. *Nat. Mater.* **2014**, *13*, 466–470. [[CrossRef](#)] [[PubMed](#)]
32. Tafti, F.F.; Gibson, Q.D.; Kushwaha, S.K.; Haldolaarachchige, N.; Cava, R.J. Resistivity plateau and extreme magnetoresistance in LaSb. *Nat. Phys.* **2016**, *12*, 272–277. [[CrossRef](#)]
33. Wolgast, S.; Kurdak, Ç.; Sun, K.; Allen, J.W.; Kim, D.-J.; Fisk, Z. Low-temperature surface conduction in the Kondo insulator SmB₆. *Phys. Rev. B* **2013**, *88*, 180405. [[CrossRef](#)]
34. Kim, D.J.; Thomas, S.; Grant, T.; Botimer, J.; Fisk, Z.; Xia, J. Surface Hall Effect and Nonlocal Transport in SmB₆: Evidence for Surface Conduction. *Sci. Rep.* **2013**, *3*, 3150. [[CrossRef](#)] [[PubMed](#)]
35. Li, Y.; Li, L.; Wang, J.; Wang, T.; Xu, X.; Xi, C.; Cao, C.; Dai, J. Resistivity plateau and negative magnetoresistance in the topological semimetal TaSb₂. *Phys. Rev. B* **2016**, *94*, 121115. [[CrossRef](#)]
36. Saleheen, A.I.U.; Chapai, R.; Xing, L.; Nepal, R.; Gong, D.; Gui, X.; Xie, W.; Young, D.P.; Plummer, E.W.; Jin, R. Evidence for topological semimetallicity in a chain-compound TaSe₃. *npj Quantum Mater.* **2020**, *5*, 53. [[CrossRef](#)]
37. Pavlosiuk, O.; Swatek, P.; Wiśniewski, P. Giant magnetoresistance, three-dimensional Fermi surface and origin of resistivity plateau in YSb semimetal. *Sci. Rep.* **2016**, *6*, 38691. [[CrossRef](#)]
38. An, L.; Zhu, X.; Gao, W.; Wu, M.; Ning, W.; Tian, M. Chiral anomaly and nontrivial Berry phase in the topological nodal-line semimetal SrAs₃. *Phys. Rev. B* **2019**, *99*, 045143. [[CrossRef](#)]
39. Laha, A.; Mardanya, S.; Singh, B.; Lin, H.; Bansil, A.; Agarwal, A.; Hossain, Z. Magnetotransport properties of the topological nodal-line semimetal CaCdSn. *Phys. Rev. B* **2020**, *102*, 035164. [[CrossRef](#)]
40. Wang, Y.L.; Thoutam, L.R.; Xiao, Z.L.; Hu, J.; Das, S.; Mao, Z.Q.; Wei, J.; Divan, R.; Luican-Mayer, A.; Crabtree, G.W.; et al. Origin of the turn-on temperature behavior in WTe₂. *Phys. Rev. B* **2015**, *92*, 180402. [[CrossRef](#)]
41. Wang, Y.-Y.; Yu, Q.-H.; Guo, P.-J.; Liu, K.; Xia, T.-L. Resistivity plateau and extremely large magnetoresistance in NbAs₂ and TaAs₂. *Phys. Rev. B* **2016**, *94*, 041103. [[CrossRef](#)]
42. Xing, L.; Chapai, R.; Nepal, R.; Jin, R. Topological behavior and Zeeman splitting in trigonal PtBi_{2-x} single crystals. *npj Quantum Mater.* **2020**, *5*, 10. [[CrossRef](#)]
43. Singha, R.; Pariari, A.K.; Satpati, B.; Mandal, P. Large nonsaturating magnetoresistance and signature of nondegenerate Dirac nodes in ZrSiS. *Proc. Natl. Acad. Sci. USA* **2017**, *114*, 2468–2473. [[CrossRef](#)] [[PubMed](#)]
44. Kumar, P.; Patnaik, S. Origin of exceptional magneto-resistance in Weyl semimetal TaSb₂. *J. Phys. Commun.* **2019**, *3*, 115007. [[CrossRef](#)]
45. Ali, M.N.; Schoop, L.; Xiong, J.; Flynn, S.; Gibson, Q.; Hirschberger, M.; Ong, N.P.; Cava, R.J. Correlation of crystal quality and extreme magnetoresistance of WTe₂. *Europhys. Lett.* **2015**, *110*, 67002. [[CrossRef](#)]
46. Zhu, Z.; Lin, X.; Liu, J.; Fauqué, B.; Tao, Q.; Yang, C.; Shi, Y.; Behnia, K. Quantum Oscillations, Thermoelectric Coefficients, and the Fermi Surface of Semimetallic WTe₂. *Phys. Rev. Lett.* **2015**, *114*, 176601. [[CrossRef](#)]
47. Ali, M.N.; Xiong, J.; Flynn, S.; Tao, J.; Gibson, Q.D.; Schoop, L.M.; Liang, T.; Haldolaarachchige, N.; Hirschberger, M.; Ong, N.P.; et al. Large, non-saturating magnetoresistance in WTe₂. *Nature* **2014**, *514*, 205–208. [[CrossRef](#)]
48. Kopelevich, Y.; Pantoja, J.C.M.; da Silva, R.R.; Moehlecke, S. Universal magnetic-field-driven metal-insulator-metal transformations in graphite and bismuth. *Phys. Rev. B* **2006**, *73*, 165128. [[CrossRef](#)]
49. Khveshchenko, D.V. Magnetic-Field-Induced Insulating Behavior in Highly Oriented Pyrolytic Graphite. *Phys. Rev. Lett.* **2001**, *87*, 206401. [[CrossRef](#)]
50. Thoutam, L.R.; Wang, Y.L.; Xiao, Z.L.; Das, S.; Luican-Mayer, A.; Divan, R.; Crabtree, G.W.; Kwok, W.K. Temperature-Dependent Three-Dimensional Anisotropy of the Magnetoresistance in WTe₂. *Phys. Rev. Lett.* **2015**, *115*, 046602. [[CrossRef](#)]
51. Narayanan, A.; Watson, M.D.; Blake, S.F.; Bruyant, N.; Drigo, L.; Chen, Y.L.; Prabhakaran, D.; Yan, B.; Felser, C.; Kong, T.; et al. Linear Magnetoresistance Caused by Mobility Fluctuations in *n*-Doped Cd₃As₂. *Phys. Rev. Lett.* **2015**, *114*, 117201. [[CrossRef](#)] [[PubMed](#)]
52. Pippard, A.B. *Magnetoresistance in Metals*; Cambridge University Press: Cambridge, UK, 1989; Volume 2.
53. Feng, D.; Jin, G. *Introduction To Condensed Matter Physics*; World Scientific Publishing Company: London, UK, 2005; Volume 1.
54. Fallah Tafti, F.; Gibson, Q.; Kushwaha, S.; Krizan, J.W.; Haldolaarachchige, N.; Cava, R.J. Temperature-field phase diagram of extreme magnetoresistance. *Proc. Natl. Acad. Sci. USA* **2016**, *113*, E3475–E3481. [[CrossRef](#)] [[PubMed](#)]

55. Han, F.; Xu, J.; Botana, A.S.; Xiao, Z.L.; Wang, Y.L.; Yang, W.G.; Chung, D.Y.; Kanatzidis, M.G.; Norman, M.R.; Crabtree, G.W.; et al. Separation of electron and hole dynamics in the semimetal LaSb. *Phys. Rev. B* **2017**, *96*, 125112. [[CrossRef](#)]
56. Pavlosiuk, O.; Swatek, P.; Kaczorowski, D.; Wiśniewski, P. Magnetoresistance in LuBi and YBi semimetals due to nearly perfect carrier compensation. *Phys. Rev. B* **2018**, *97*, 235132. [[CrossRef](#)]

Disclaimer/Publisher's Note: The statements, opinions and data contained in all publications are solely those of the individual author(s) and contributor(s) and not of MDPI and/or the editor(s). MDPI and/or the editor(s) disclaim responsibility for any injury to people or property resulting from any ideas, methods, instructions or products referred to in the content.